

# High Sensitive Vectorial $\dot{B}$ -probe for Low Frequency Plasma Waves

Stefan Ullrich,\* Olaf Grulke, Thomas Klinger, and Kian Rahbarnia  
*Max-Planck-Institut für Plasmaphysik, EURATOM Association,  
Wendelsteinstraße 1, 17491 Greifswald, Germany*

A miniaturized multidimensional magnetic probe is developed for application in a low-temperature plasma environment. A very high sensitivity for low-frequency magnetic field fluctuations with constant phase run, a very good signal-to-noise ratio combined with an efficient electrostatic pickup rejection renders the probe superior compared with any commercial solution. A two-step calibration allows for absolute measurement of amplitude and direction of magnetic field fluctuations. The excellent probe performance is demonstrated by measurements of the parallel current pattern of coherent electrostatic drift wave modes in the VINETA experiment.

PACS numbers: 52.35.Kt, 52.25.Xz, 07.55.-w, 52.70.Ds

## I. INTRODUCTION AND EXPERIMENTAL SETUP

Magnetic induction probes, so-called  $\dot{B}$ -probes, are the fundamental tool for measurements of magnetic field fluctuations in a broad variety of systems ranging from small-scale laser-produced plasmas [1] to large-scale fusion devices [2]. Although the measurement principle in all those systems remains essentially unchanged the detailed design needs to account for the specific situation. A major challenge is to achieve a high signal-to-noise ratio (SNR) at small size to minimize plasma disturbance by the probe with adequate capacitive pick-up rejection. Various authors have presented developments of  $\dot{B}$ -probes particularly for medium to high frequency magnetic fluctuation measurements. In this regime capacitive pickup can be efficiently rejected using center-tapped transformers [3, 4]. For small frequency fluctuations the signal has to be measured differentially, preferentially close to the probe head, which counteracts with the requirements of small size. This paper presents a highly sensitive multidimensional compact  $\dot{B}$ -probe for measurements of the current pattern of low-frequency waves and instabilities. The probe has been successfully used to measure the dispersion relation of Alfvén wave [5]. In the present paper the performance is demonstrated by measurements of the axial current pattern of coherent drift wave modes in the linear helicon device VINETA. Since drift waves in the highly collisional helicon plasma develop as electrostatic drift waves [6], the associated parallel electron current density and thus the frequency is much smaller than in the case of Alfvén waves. This use case sets the ambitious design target of the probe. The paper is organized as follows: In Sec. II the experimental setup and the plasma parameter regime is briefly outlined. In Sec. III the principle characteristic of  $\dot{B}$ -probes is compared to alternative magnetic diagnostic schemes, i.e. a magnetoresistive sensor and a commercial Hall probe. The detailed

TABLE I. Operational parameters of VINETA

parameter	value
magnetic field $B_0$	50 mT
peak electron temperature $T_e$	$\approx 2$ eV
ion temperature $T_i$	0.2 eV
plasma density $n$	$\lesssim 10^{19} \text{ m}^{-3}$
plasma- $\beta$	1%

construction and electronic circuit of the  $\dot{B}$ -probe together with its calibration is presented in Sec. IV. The plasma current reconstruction is based on the simultaneous measurement of all magnetic field components as presented in Sec. V, which allows for the detailed investigation of the current pattern associated with coherent drift wave modes, Sec. VI. Special attention is paid to a directional *in situ* calibration of the individual probe coils in a well-known test magnetic field.

## II. EXPERIMENTAL SETUP AND PLASMA PARAMETER REGIME

The experimental device VINETA[7] is schematically shown in Fig. 1. The vacuum vessel has a length of 4.5 m and a diameter of 0.4 m. It is embedded into a system of magnetic coils able to generate a magnetic field with  $B_0 \leq 0.1$  T. As working gas argon is used. The plasma is generated by a helical  $m = 1$  helicon antenna [8], which is operated by a pulsed transmitter at a frequency of 13.56 MHz with an output power of typically  $P = 1.5$  kW. Resulting plasma parameters are compiled in Tab. I.

It has been shown in previous investigations that drift waves are unstable in the used configuration and occur as single coherent modes [6]. The frequency of the observed drift modes in VINETA is in the range  $1 \dots 10$  kHz with typical amplitudes of the density fluctuations of  $\tilde{n}/n = 1\%$  [9]. For drift waves the absolute amplitude of magnetic field fluctuation can be estimated using the scaling with  $\beta$  as fraction of kinetic to magnetic pressure

\* present address: post@ullrich-engineering.de

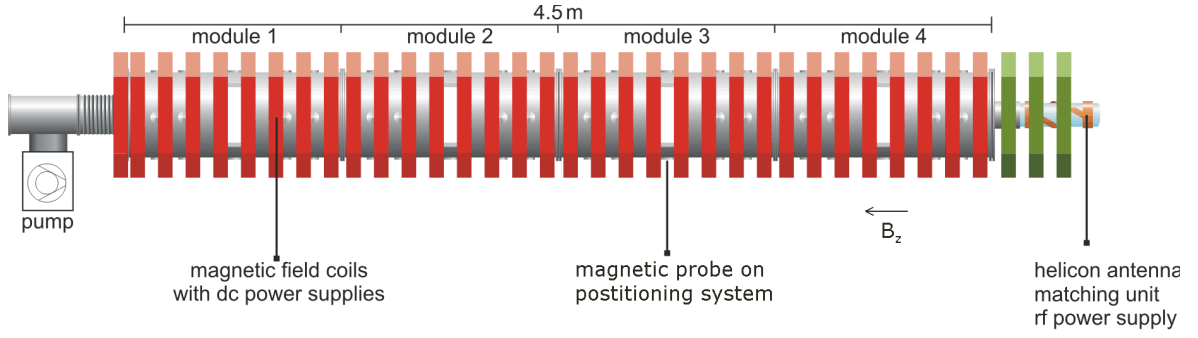


FIG. 1. Schematic of the VINETA experiment with the positioning system for wave detection.

[10]

$$\frac{b}{B_0} \approx \beta \frac{\tilde{n}}{n} \quad (1)$$

in which  $b$  denotes the fluctuating magnetic amplitude. The plasma  $\beta$  in the center of VINETA has a value of about 1 %. For  $B_0 = 50$  mT Equ. (1) yields an expected fluctuating magnetic field of  $b = 5 \mu\text{T}$ . This rough estimation is used as a design target for the sensitivity of the magnetic probe. The design target for the frequency range is 1 kHz ... 1 MHz to cover the frequency range of drift- and Alfvén waves in VINETA [5, 9].

### III. COMPARISON OF DIFFERENT MAGNETIC SENSORS

The probe is designed to resolve magnetic fluctuations in the range of  $b = 1 \mu\text{T}$ . For this task different sensor technologies can be used. A recent review is found in [11, 12], which compares 11 different sensor types. Most of them can be excluded due to the sensitivity and the size limitations for a small plasma probe. Two sensor types can be considered as suitable candidates for the given task, the  $\dot{B}$  sensor, and the magneto-resistive sensor. Additionally, the Hall sensor is also considered and tested even though its sensitivity is much smaller than for the other sensor types. However, in previous work it was successfully used as low-frequency magnetic detector in the edge of fusion plasmas [13, 14]. Table II compiles the three tested devices. The magneto resistive sensor and the Hall sensor are available through standard distributors for electronic parts. All sensors are operated with low noise amplifiers, the Hall sensor is additionally connected to a current source. For the  $\dot{B}$  sensor a filter and adaptation network is used at the amplifier input.

To compare the sensors, their sensitivity  $S$  is measured as function of frequency  $\omega$

$$b = S(\omega) \cdot U \quad (2)$$

The complex amplitude of the measured output voltage  $U$  corresponds to the complex amplitude of the fluctuating magnetic field  $b$ . To record  $S(\omega)$  a test field

consisting of two coils with a diameter of 78 mm, four windings each, and 35 mm separated from each other, is used. The test field amplitude in the center of the coil is  $b = 2 \mu\text{T}$ . The sensor calibration is performed by automatically sweeping the frequency while the sensor is located in the center between the test field coils. The current through the test field coils and the output voltage of the sensor are simultaneously recorded and evaluated.

The obtained sensitivity  $S(\omega)$  alone is not meaningful for comparing different sensors. Using external or internal amplifiers,  $S(\omega)$  can take any value for the same device and does not refer to the smallest detectable amplitude. The smallest detectable amplitude is actually limited by the noise figure of a certain sensor-amplifier combination. It is measured by recording the sensor signal of 100 ms duration with a high sampling rate of  $f_{\text{smpi}} = 10$  MHz with no magnetic field fluctuation present. The power spectral density of this quiescence signal, obtained by Fourier transformation and subsequent averaging, is a frequency-resolved measure for the noise density

$$u_{\text{noise}}(\omega) = \frac{1}{2\pi} \int U_{\text{noise}}(t) e^{-i\omega t} dt \quad (3)$$

If a certain frequency window  $\Delta f$  is assumed, the noise voltage is obtained as

$$U_{\text{noise}}(\omega) = u_{\text{noise}}(\omega) \cdot \Delta f \quad (4)$$

The signal-to-noise ratio (SNR) for a given magnetic field amplitude  $b$  is consequently defined as

$$\text{SNR} = 20 \log \left( \frac{b}{U_{\text{noise}} S} \right) \quad (5)$$

In the following a frequency window of  $\Delta f = 100$  Hz is assumed. This is equal to an integration time of 10 ms and limits the observable fluctuations to frequencies above 100 Hz in agreement with the design target given above. The frequency-resolved results for the three sensor types are depicted in Fig. 2 in terms of (a)  $S(\omega)$  and (b)  $\text{SNR}(\omega)$ .

The resulting sensitivity is constant for the magneto resistive sensor, as expected from the data sheet. The

TABLE II. Tested sensor devices for measurement of magnetic field fluctuations

manufacturer	device	sensor type	dimension [mm <sup>3</sup> ]	distributor
Infineon	KSY14	Hall sensor	6	www.sh-halbleiter.de
Honeywell	HMC1001	magneto-resistive sensor	80	www.farnell.com
(self-made)	coil N=1000	$\dot{B}$ sensor	38	—

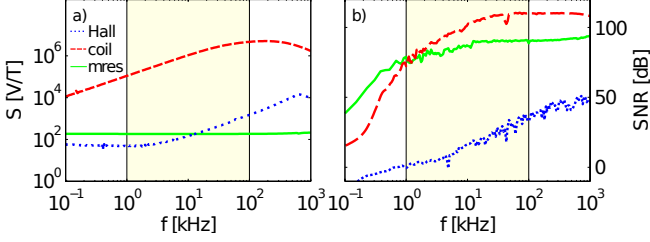


FIG. 2. Frequency response of the tested Hall sensor, the magneto-resistive sensor, and the  $\dot{B}$  sensor with low noise amplifier. In (a) the frequency-resolved sensitivity of the devices is shown, in (b) the signal-to-noise ratio. The highlighted frequency range indicates the intended operation regime of the probe in VINETA from 1...100 kHz.

sensitivity of the  $\dot{B}$  sensor has a linear slope of 3 dB per octave below 10 kHz due to the time derivative in the induction law and reaches a maximum around 200 kHz. This is the broadly damped self-resonance peak of the used coil (c.f. Sec. IV). The sensitivity of the Hall sensor is constant for frequencies below 2 kHz and increases for higher frequencies with 3 dB per octave. This might be an indication that the signal from the wiring loop with  $N=1$  to the sensor is larger than the expected constant Hall voltage. For the SNR a magnetic field amplitude of  $b = 1 \mu\text{T}$  is assumed as the necessary resolution limit for the expected magnetic fluctuation levels. The best performance within the operation frequency range shows the  $\dot{B}$  sensor with a SNR exceeding 100 dB. This result clearly demonstrates that the  $\dot{B}$  sensor is the best choice for the specified design parameter range.

#### IV. $\dot{B}$ -PROBE: WIRING CONCEPT AND PERFORMANCE

The key issues of a  $\dot{B}$ -probe immersed into a plasma are the small induced voltages in an environment of large fluctuating electric fields [3] and the possibility of charging up to the (fluctuating) floating potential. Both failure mechanisms lead to signal parts not originating from magnetic field fluctuations. The probe's voltage response is proportional to the windings of the coil. However, increasing the number of windings is limited by (1) the requirements for a small size of the probe and (2) the self-resonance of the coil. Using a thin copper wire with diameter  $50 \mu\text{m}$ , a coil with 3 mm diameter and 8 mm length carries  $N = 1000$  windings. The electrical capacity between windings together with

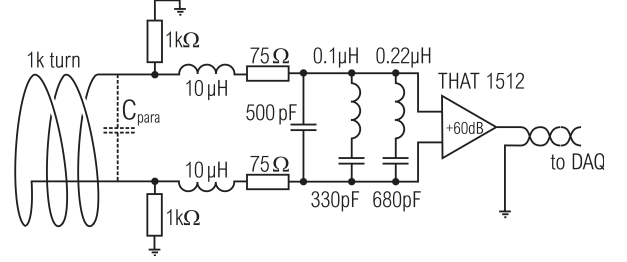


FIG. 3. Filter and attenuation network for connecting one detection coil to the low-noise amplifier.

the inductance of the coil forms a resonance circuit with a resonance frequency  $f_{\text{reso}} = 100 \text{ kHz}$  for the actual design. When calibrating the probe, the sharp resonance peak leads to a large uncertainty in the sensitivity around  $f_{\text{reso}}$ . To avoid this, the resonance is symmetrically damped in our design with  $2 \times 1 \text{ k}\Omega$  resistors, directly at the amplifier input. The resonance peak is then broadened and a well defined sensitivity can be determined. The resulting induced voltage is  $44 \mu\text{V}$  for  $f = 1 \text{ kHz}$  and  $b = 1 \mu\text{T}$ . In some experiments the plasma potential fluctuations can reach several Volt or more [15, 16]. The probe head and the transmission line are capacitively coupled to the plasma potential so that plasma potential fluctuations are superimposed to the magnetic signal as electrostatic pickup. For minimizing electrostatic pickup and to prevent the probe from charging up to the floating potential, the probe head, the transmission line, and the amplifier have a symmetrical design and are covered with a grounded shielding. Special attention is paid to connect all shielding parts as tight as possible to prevent any penetration of the plasma to the active parts of the probe. Additionally, the amplifier is located as close as possible to the probe head, about 15 cm outside the core plasma, still inside the vacuum vessel. This keeps transmission lines short and minimized the parasitic capacity between lines and plasma.

For amplifying the recorded signal the low-noise SMD-amplifier THAT1512 is chosen, which is designed for high-end audio applications. Its input referenced noise figure equals the expected thermal noise from a  $200 \Omega$  resistor at room temperature. The amplification is +60 dB, the bandwidth is  $f_{\text{bw}} = 1 \text{ MHz}$ . Although the bandwidth is much larger than any expected frequency of waves under investigation, it is important to remove any signal parts above that frequency limit to avoid distortions in the amplifier. In particular the rf

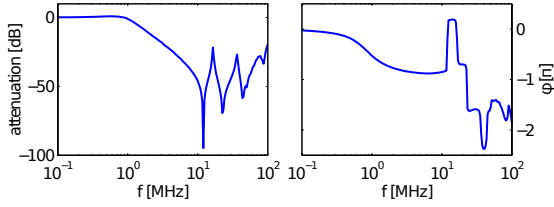


FIG. 4. Measured transfer function in terms of (a) amplitude and (b) phase of the rf-protection input filter without amplifier.

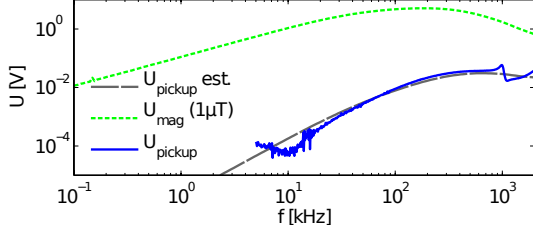


FIG. 5. Electrostatic pickup measurement of the  $\dot{B}$ -probe. The blue curve shows the equivalent magnetic field reading for an electric field of 5 V/cm. The green curve shows the expected output voltage for a fluctuating magnetic field with constant amplitude of 1  $\mu$ T (design-target). The gray curve is the expected magnetic fluctuation amplitude generated by the currents into the test field capacitor.

plasma generation frequency of  $f_{rf} = 13.56$  MHz has to be damped. The filtering circuit for this purpose is given in Fig. 3. After being damped by the  $2 \times 1$  k $\Omega$  resistors, the signal is symmetrically low pass filtered ( $2 \times L = 10$   $\mu$ H,  $2 \times R = 75$   $\Omega$ ,  $C = 100$   $\mu$ H) with  $f_{-3dB} = 1$  MHz and passed on to two notch filters at  $f_{rf}$  and  $2f_{rf}$ .

The result of a measurement of the filter transfer function as attenuation and phase response is shown in Fig. 4. Below 1 MHz the attenuation is close to 0 dB and the signal phase changes only slightly without any phase jumps. This is the measurement frequency range with negligible effect of the filter. Drift and Alfvén waves are observed well below 100 kHz in VINETA. Up to 10 MHz the filter transfer function decays with 6 dB per octave as expected for an LC-filter. At  $f_{rf}$  and  $2f_{rf}$  the input signal is strongly damped to values  $< -70$  dB.

After assembling the probe with shielding, filter and amplifier, the frequency resolved sensitivity and SNR was recorded. The result is shown in Fig. 2(a) and 2(b). In a wide frequency range a SNR exceeding 100 dB is reached. To get a measure for the sensitivity of the probe for electrostatic pickup the probe was placed in the homogeneous electric field of a parallel plate capacitor. The capacitor was driven by a swept voltage generating electric fields with amplitudes of 5 V/cm in the frequency range up to 2 MHz. The frequency-dependent signal amplitude from the probe is shown in Fig. 5. It has a linear slope up to  $f = 100$  kHz, saturates, and then decreases. The output voltage for an assumed con-

stant magnetic fluctuation of 1  $\mu$ T as design-target is included for comparison. It is 20...40 dB larger than the measured electrostatic pickup. Although this is already a reasonable value for the suppression of electrostatic pickup, the origin of measured amplitude is most likely the magnetic field of the displacement current into the capacitor  $I_\omega = \omega U/C$ . An estimation is included in Fig. 5, which considers the frequency response of the  $\dot{B}$ -detector. The measured signal agrees quite well with this estimate. Thus, the capacitive pickup can be neglected in the following.

## V. PROBE FOR VECTOR FIELD DETECTION

To allow for detection of three vector field components  $b_x, b_y, b_z$  multiple coils are integrated into the shielded probe head as shown in the photograph, Fig. 6. Two coils for the perpendicular magnetic components  $b_x$  and  $b_y$  are located in the middle part of the probe with their coil surface normals oriented perpendicularly to each other. The coils have a diameter of 3 mm and a length of 8 mm. To conserve symmetry, the third coil for the parallel magnetic component  $b_z$  is split into two equal parts and surrounds the two perpendicular coils. Each of the four coils is separately connected via a twisted pair wire to one amplifier channel including filter and adaptation network. The probe head is electrically shielded by a brass cylinder. The insulation from the plasma is achieved with an ceramic cylinder. A PT100 temperature sensor is integrated into the probe head to monitor the operation temperature and turn off the plasma generation when exceeding a temperature threshold.  $T = 120^\circ$  turned out to reasonably protect the windings from melting.

The calibration of the probe is done in two steps. First the complex sensitivity  $S(\omega)$  of each of the four pickup coils as fully assembled probe is recorded as described in Sec. III. In particular the phase shift introduced by the magnetic field penetrating into the probe head is here considered. For practical reasons it is difficult to measure the exact directions of the coil surface normals, which have a strong influence in the three-dimensional magnetic field reconstruction. Instead as second calibration step a directional calibration is performed, which allows to reconstruct the magnetic fluctuations in Cartesian coordinates  $b_x, b_y$  and  $b_z$ . The directional calibration is performed by measuring the well defined magnetic field of a cylindrical test coil along a grid in front of the test coil. For each Cartesian component the magnetic field reads

$$b_x = S_1^x U_1 + S_2^x U_2 + \dots S_n^x U_n \quad (6)$$

$$b_y = S_1^y U_1 + S_2^y U_2 + \dots S_n^y U_n \quad (7)$$

$$b_z = S_1^z U_1 + S_2^z U_2 + \dots S_n^z U_n, \quad (8)$$

or in short

$$\vec{b} = A_{cal} \vec{U}. \quad (9)$$



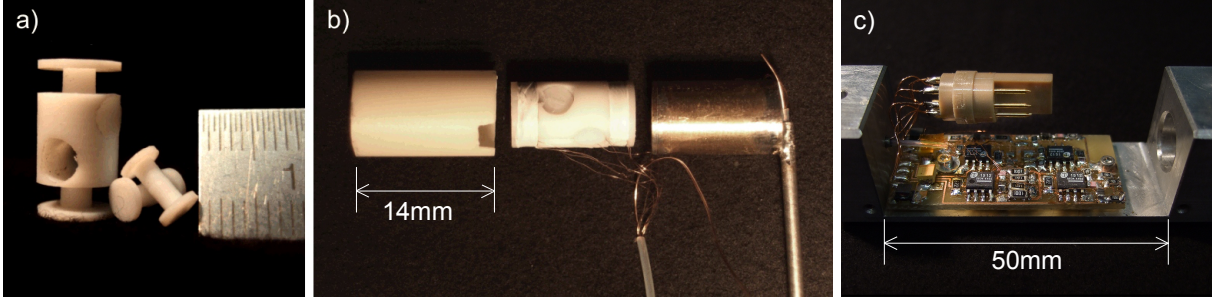


FIG. 6. Design of a vectorial  $\dot{B}$ -probe. (a) shows the probe body and the small perpendicular coils. (b) is a photo of a finished probe head, consisting of the plasma facing ceramic tube (left), the probe body with readily wound coils (middle) and the electrical shielding (right) which is connected to ground. (c) shows the amplifier with matching network in the opened shielding box

where  $U_x$  is the voltage of channel  $x$ . The number  $n$  of coils is four in the case of our  $\dot{B}$ -probe. Each component of  $A_{\text{cal}}$  converts a voltage to a magnetic field and is thus a sensitivity. The tensor can be split into two parts

$$A_{\text{cal}} = A_{\text{dcal}} A_{\text{fcal}}, \quad (10)$$

where  $A_{\text{dcal}}$  is a  $3 \times 3$  matrix for directional calibration and  $A_{\text{fcal}}$  a  $3 \times n$  matrix for sensitivity calibration. The latter one has  $n$  non-zero elements which are derived from the frequency calibration described above, one for each coil. Experimentally, the matrix  $A_{\text{dcal}}$  is obtained by comparing the measured magnetic field  $\vec{b}_{\text{meas}} = A_{\text{fcal}} \vec{U}$  with the known field  $\vec{b}$ . Since this vector equation has three components and  $A_{\text{dcal}}$  has 9 elements, three spatial points of the calibration field are sufficient. They have to be chosen in such a way that the involved magnetic field vectors span a non-degenerated three-dimensional space to form 3 linearly independent equations. The 3 equations can be written as

$$\begin{pmatrix} b_x^1 & b_x^2 & b_x^3 \\ b_y^1 & b_y^2 & b_y^3 \\ b_z^1 & b_z^2 & b_z^3 \end{pmatrix} = \begin{pmatrix} A_{11} & A_{12} & A_{13} \\ A_{21} & A_{22} & A_{23} \\ A_{31} & A_{32} & A_{33} \end{pmatrix} \begin{pmatrix} b_{mx}^1 & b_{mx}^2 & b_{mx}^3 \\ b_{my}^1 & b_{my}^2 & b_{my}^3 \\ b_{mz}^1 & b_{mz}^2 & b_{mz}^3 \end{pmatrix}. \quad (11)$$

The unknown directional calibration matrix is obtained by multiplying the inverse of the matrix of the measured magnetic field  $b_m$  from the right

$$A_{\text{dcal}} = \hat{b} \cdot \hat{b}_m^{-1}. \quad (12)$$

In our case an azimuthal plane in front of a cylindrical test coil with a diameter of  $d = 100$  mm and  $N = 53$  windings was scanned with the magnetic probe with a spatial resolution of 1 cm. The field of the coil is calculated using Biot-Savart law. To ensure the linear independence of the equations, three magnetic field vectors are chosen, spanning a parallelepiped  $(\vec{b}_1, \vec{b}_2, \vec{b}_3)$  with a

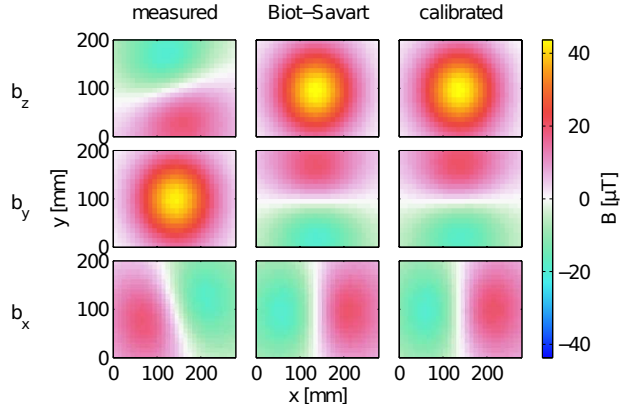


FIG. 7. Directional calibration scan of the vectorial  $\dot{B}$  probe with freely chosen probe orientation. The left column shows three channels of the raw measurement. In the middle column the expected field calculated with Biot-Savart law is given. The right column shows the measured components  $b_x, b_y, b_z$  after application of the directional calibration.

volume above a certain threshold.  $A_{\text{dcal}}$  is calculated several times in this way and allows one also to extract the error of this procedure for every component of  $A_{\text{dcal}}$ . The result of a calibration scan is depicted in Fig. 7. The diagrams in the middle column show the calculated magnetic field. The field has a maximum in the  $z$ -component along the axis of the coil and flips from positive to negative values for the perpendicular components  $b_x$  and  $b_y$ . The coil normals corresponding to the three components of the measured field in the first column are chosen randomly. The recorded field pattern is shifted and tilted in comparison with the known field. The channels even seem to be interchanged, what should be considered in the current context as strong tilting of the corresponding coil. The presented algorithm corrects all of these positioning errors. As shown in the right column the calibrated field reproduces well the known field. Since the calibration matrix  $A_{\text{dcal}}$  is calculated from only three magnetic vectors out of the

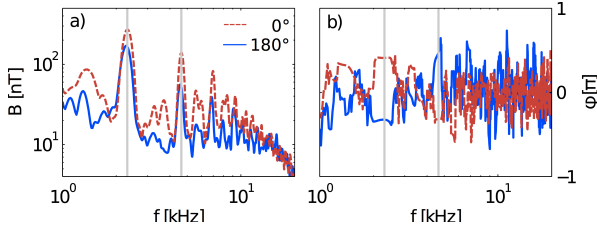


FIG. 8. Magnetic fluctuation spectrum of drift waves with (a) amplitude and (b) phase run. The red and blue curves show the spectrum for the probe rotated by  $180^\circ$  with all other parameters kept constant.

plane, this procedure is not a fit from the measured to the theoretically derived magnetic field.

## VI. MAGNETIC COMPONENTS AND PARALLEL CURRENT OF COHERENT DRIFT WAVES MODES

The magnetic probe is used to characterize magnetic field fluctuations associated with drift waves [17]. As gradient driven instability they occur in the steep plasma density gradients of the cylindrical plasma discharge of VINETA [18]. At these locations drift waves are observed as fluctuations of the plasma density of up to 10% [9]. On a microscopic scale perpendicular ion polarization currents are balanced by fluctuating parallel electron currents, which represent a footprint of the three-dimensional dynamic of the drift wave and stand in contrast to fluid-like instabilities, e.g. the Kelvin-Helmholtz instability. The signal from the magnetic probe was recorded together with a reference signal from a Langmuir probe, both positioned in the gradient region. The frequency spectrum of the signal of one component  $b_x$  of the magnetic probe is shown in Fig. 8. A clear peak in the amplitude spectrum is observed at the frequency of the drift wave  $f = 2.3 \text{ kHz}$  and its higher harmonics with a well defined phase. When the probe is rotated by  $180^\circ$  around the y-axis the amplitude spectrum remains essentially unchanged, whereas the phase at the peaks in the spectrum changes by  $\pi$ . This fact proves that electrostatic pickup of the drift wave potential fluctuations including charging up of active probe parts to the floating potential does not contribute significantly to the spectrum. The peak magnetic field amplitude is small with  $\approx 0.2 \mu\text{T}$ . The systematic difference in the amplitude spectrum is most probably an effect of the unavoidable position change of the probe head when rotating by  $180^\circ$ .

To reconstruct the spatiotemporal evolution of the fluctuating magnetic field of a coherent drift wave mode, measurements of the magnetic field and plasma density fluctuations in an entire azimuthal plane have been done. One Langmuir probe located at a fixed position in the maximum radial plasma density gradient region,

which measures the plasma density fluctuations of the drift wave mode, is used as a phase reference. The reconstruction of the density fluctuation pattern in the azimuthal plane shows a  $m=3$  drift wave mode, which propagates into the electron diamagnetic drift direction, which is clockwise in the representation Fig. 9(a).

In Fig. 9(b) the result is shown for the perpendicular components of the fluctuating magnetic field. As expected for a  $m = 3$  drift wave mode, 6 current filaments with alternating signs are clearly visible. The recorded magnetic field fluctuations of the absolutely calibrated probe are used to calculate the parallel current components  $j_z$  with Ampère's law

$$\mu_0 j_z = \frac{\partial b_y}{\partial x} - \frac{\partial b_x}{\partial y}. \quad (13)$$

The result is shown in Fig. 9(c). The maxima and minima of the currents are at the same positions as the corresponding density fluctuations. The peak drift wave mode current density is  $j_{DW} \simeq 50 \text{ mA/cm}^2$ . These findings are in agreement with the local slab model of drift waves, where parallel currents are driven by parallel pressure gradients [19]. A quantitative analysis of the parallel force balance equation [20] in the given collisional low-temperature plasma of VINETA reveals the observation as so-called electrostatic drift waves.

## VII. SUMMARY

A highly sensitive magnetic  $\vec{B}$ -probe is developed for application in the low temperature argon plasma of VINETA. Drift waves as low frequency plasma instability and Alfvén waves define the ambitious design criteria for the  $\vec{B}$ -probe in terms of the frequency range, the necessary sensitivity and the size of the probe head. Much effort is spent to avoid electrostatic pickup and to reconstruct the vectorial magnetic field fluctuations in Cartesian coordinates with a directional calibration method. The ready built probe with a SNR higher than 100 dB, a frequency range of  $f = 100 \text{ Hz} \dots 1 \text{ MHz}$  and a miniaturized probe head is undoubtedly preferable to commercially available solutions. As first application the fluctuating magnetic field of a coherent drift mode is recorded with the  $\vec{B}$ -probe. The excellent quality of the recorded magnetic fluctuation data allows for a clear reconstruction of the current filaments associated with the drift mode.

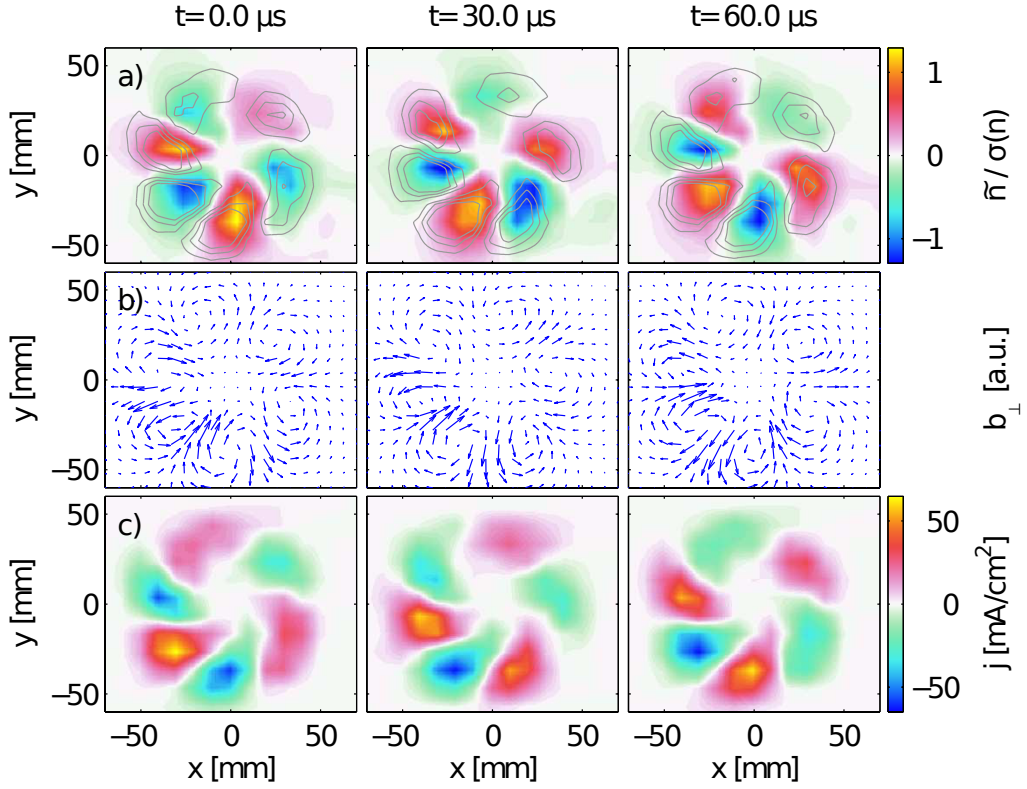


FIG. 9. Combined magnetic field and density fluctuation scan of a  $m = 3$  drift wave mode in azimuthal plane. The ambient magnetic field points into the plane. Fields and currents are shown for three time instants with  $\Delta t = T/4$ . (a) shows the density fluctuations, superposed with the isolines of the parallel current density  $j_{\parallel}$  in (c) at the levels  $-30, -20, \dots, +20 \text{ mA/cm}^2$ . The direction of the measured magnetic field components  $b_x$  and  $b_y$  is shown in (b).

- 
- [1] E. T. Everson, P. Pribyl, C. G. Constantin, A. Zylstra, D. Schaeffer, N. L. Kugland and C. Niemann Rev. Sci. Instrum. **80**, 113505 (2009).
  - [2] E. J. Strait Phys. Plasma **77**, 023502 (2006).
  - [3] C. M. Franck, O. Grulke, and T. Klinger, Rev. Sci. Instrum. **73**, 3768 (2002).
  - [4] B. Sun, G. Y. Yuan, W. G. Huo, and Z. F. Ding Rev. Sci. Instrum. **81**, 054703 (2010).
  - [5] K. Rahbarnia, S. Ullrich, K. Sauer, O. Grulke, and T. Klinger, Phys. Plasmas **17**, 032102 (2010).
  - [6] C. Schröder, O. Grulke, T. Klinger, and V. Naulin, Phys. Plasma **11**, 4249 (2004).
  - [7] C. M. Franck, O. Grulke, and T. Klinger, Phys. Plasma **9**, 3254 (2002).
  - [8] R. W. Boswell. Plasma Phys. Controlled Fusion **26**, 1147 (1984).
  - [9] C. Schröder, O. Grulke, T. Klinger, and V. Naulin, Phys. Plasmas **12**, 042103 (2005).
  - [10] K. Rahbarnia, E. Holzhauser, N. Mahdizadeh, M. Rammisch, and U. Stroth, Plasma Phys. Controlled Fusion **50**, 085008 (2008).
  - [11] J. E. Lenz and A. S. Edelstein, IEEE Sens. J. **6**, 631 (2006).
  - [12] J. E. Lenz, Proc. IEEE **78**, 973 (1990).
  - [13] I. Duran, J. Stockel, G. Mank, K. H. Finken, G. Fuchs, and G. V. Oost, Rev. Sci. Instrum. **73**, 3482 (2002).
  - [14] Y. H. Liu, D. A. Maurer, G. A. Navratil, and N. Rivera, Rev. Sci. Instrum. **76**, 093501 (2005).
  - [15] J. L. Holt, N. C. Luhmann, and J. T. Tang, J. Appl. Phys. **47**, 4467 (1976).
  - [16] M. J. Burin, G. R. Tynan, G. Y. Antar, N. A. Crocker, and C. Holland Phys. Plasma **12**, 052320 (2005).
  - [17] J. T. Tang and N. C. Luhmann, Phys. Fluids **19**, 1935 (1976).
  - [18] O. Grulke, T. Windisch, C. Brandt, S. Ullrich, and T. Klinger, Plasma Fusion Res. **5**, 013-1 (2010).
  - [19] H. W. Hendel, T. K. Chu, and P. A. Politzer, Phys. Fluids **11**, 2426 (1968).
  - [20] B. D. Scott, Contrib. Plasma Phys. **46**, 714 (2006).